Dual-Arm Compliance Control with Robust Force Decomposition

William Freidank[1,2], Konrad Ahlin[2] and Stephen Balakirsky[2]
[1]*Department of Mechanical Engineering, Georgia Institute of Technology, 801 Ferst Dr, Atlanta, Georgia, U.S.A.*
[2]*Georgia Tech Research Institute, 640 Strong Street, Atlanta, Georgia, U.S.A.*

Keywords: Dual-Arm Control, Compliance Control, Artificial Potential Field, Secant Method, Force Decomposition, Beam Method, Robot, Robotic, Manipulator.

Abstract: Realtime, compliant control of dual-arm robots has been an open area of investigation for versatile object manipulation. Recent research has focused on leader-follower, hybrid, and impedance control techniques. This paper proposes a guaranteed-convergence artificial potential field in order to leverage its advantages in computational speed and functional quality. Additionally, compliance control is integrated using a novel force decomposition method. Experiments are performed on a 14 Degree-of-Freedom (DoF) dual-carriage rail, with two UR5e robots to validate the new method's accuracy and demonstrate the feasibility of the unified controller.

1 INTRODUCTION

Robotics have steadily gained greater responsibility in industrial settings, especially in structured and predictable assembly operations. One major challenge to broader implementation is the inability to adapt highly task-specific solutions to new objects and situations (Kousi et al., 2018). Dual-arm, compliant manipulators promise greater versatility in the push for reliably performing maintenance operations with unpredictable disturbances and features.

There are two kinds of compliance: internal and external. A human uses "external" compliance when using their arms and hands to install an object guided by a peg and socket. The force felt from the socket correcting the orientation of the peg during insertion allows the human to adjust the insertion to comply with the actual geometry. A human uses "internal" compliance when an object cannot be grabbed at anticipated positions. For example, if the object is larger due to a design change, the human will feel the object's larger size forcing the human to "comply" with a greater spacing of their arms and hands. The problem of internal compliance is unique to systems with more than one simultaneous grasp point.

In robotics, compliance control may be realized passively through innovative mechanical designs such as variable stiffness actuators (Wolf et al., 2016) or actively through more classical methods such as parallel force/position, impedance, or admittance control (Calanca et al., 2016)(Seraji, 1994). In the active case, compliant control may be seen as a form of continuous feedback force control. Compliance can be achieved at the level of the object, at the level of robot joints, or both, as explored in (Ren et al., 2021).

(Hu et al., 2021) proposed two techniques of solving the internal and external compliant forces for dual-arm compliant control: a master-slave force control and a shared force control. The master-slave technique assumes an expected force and torque at one manipulator's end-effector, reducing the number of unknown variables to only those at the other manipulator, and then solves the system uniquely. Variations of this approach have been used elsewhere (Xian et al., 2017)(Gao et al., 2022). In the second method, the shared force technique allows for object-level force commands, but suffers from an undetermined system of equations. (Song et al., 2021) explored the control of internal and external forces when employing the shared force technique. The primary challenge in question becomes properly decomposing applied forces into internal and external contributions at the robot end-effectors. Pseudoinverse-based methods have the advantage of being readily extended to k number of manipulators, as leveraged in (Song et al., 2022). (Walker et al., 1991) proposed a No-Squeeze pseudoinverse designed to yield end-effector wrenches that are free from internal effects on the object. However, their method imposes the requirement of equal load distribution, which may not correspond to real operating conditions. A further exploration was made in (Erhart and Hirche, 2015) of the problems arising frrom unintended internal wrenches produced by different pseudoinverses, presenting an an-

Freidank, W., Ahlin, K. and Balakirsky, S.
Dual-Arm Compliance Control with Robust Force Decomposition.
DOI: 10.5220/0012177300003543
In *Proceedings of the 20th International Conference on Informatics in Control, Automation and Robotics (ICINCO 2023) - Volume 1*, pages 616-623
ISBN: 978-989-758-670-5; ISSN: 2184-2809

alytically inspired parameterized inverse. In this paper, we propose a shared-force technique that avoids mathematical optimizations in favor of a closed form solution drawing upon a physically inspired analysis incorporating established models in classical statics.

A robust control methodology may use simultaneous path planning and compliance control to achieve a larger trajectory objective. However, compliant control for large or heavy objects may require the coordinated control of multiple robotic manipulators. In such high-dimensional problems, choice of a path planning method comes down to computation time as a function of algorithm complexity, which for search-based methods, such as A* and Rapidly-exploring Random Trees (RRT), increases exponentially with the dimensions of space (LaValle, 2006). Neither can reliably solve the path planning problem with real-time capability in a fourteen-dimensional space, as necessary for the robot cell used for our research.

Artificial Potential Fields (APF), which are function-based approaches to path planning, offer compelling advantages for path planning in high dimensional spaces. APF uses a goal location and obstacles to calculate a simulated "potential" function, the gradient of which acts as a pseudo-force that directs the manipulators toward the target. The complexity of the APF algorithm scales linearly with space dimensions rather than exponentially making it ideal for high DoF path planning (Khatib, 1985) (Khatib, 1986). APF has well-known disadvantages for mobile robotics (Omar et al., 2016), but these performance issues can be alleviated by adjusting the potential function using an approach called the "Secant Method" (Ahlin et al., 2018). Furthermore, APF theory can be extended to manipulators. (Kim et al., 2021) demonstrated that the Secant Method can plan for two, six-DoF manipulators to have coordinated motion. In their research, coordinated control alongside a mechanical compliance device known as a "wiffletree" allowed two manipulators to carry a payload that was heavier than either could have carried individually. In this work, we adopt insights from (Kim et al., 2021). First, the path planning will be solved in real-time at approximately 500 Hz to match the controller. (Kim et al., 2021) used this frequency to ensure that the two manipulators' end-effectors maintained the same relative position, despite variations and errors that manifested during path execution. Second, we compute the path plan in Cartesian task space and translate the commanded pseudo-force to joint space via a Jacobian transpose. Error values can thus remain in the task space domain, which improves the relevance of the error to real-world applications and eliminates the need to translate the target location to joint space.

The general formulation of a dual-arm cooperative manipulation task is sketched in Figure 1. Each manipulator may have n_i joints for a total of $n = \Sigma n_i$ degrees of freedom. A common base frame with coordinates $\{B\}$ stands as a fixed global frame for the combined system. Further coordinate frames are established for the end-effectors, $\{E1\}$ and $\{E2\}$, as well as the manipulated object, $\{O\}$. The grasp points at which each manipulator contacts the object are known *a priori*, and are prescribed as constant homogeneous transforms in the object's fixed frame, ${}^{O}\boldsymbol{T}_{G1}$ and ${}^{O}\boldsymbol{T}_{G2}$. As a matter of convention, a manipulator's end-effector is defined as the feature which should coincide with one of an object's grasp-points.

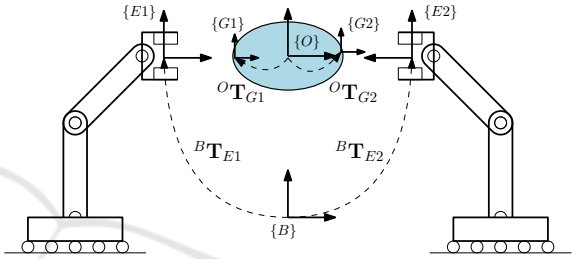

Figure 1: Dual-arm cooperative manipulation scenario.

2 COORDINATED CONTROL

2.1 Coordinated Potential Field

The combined controller should retain its capacity to direct each arm independently and allow for seamless transition from individual to cooperative manipulation. To retain independent functionality, a separate instance of the Secant controller (Ahlin et al., 2018) is initially assigned to each robot chain, forming the potential fields $\{\Psi_1, \Psi_2\}$, where each field is configured for its respective manipulator's task-space goal. In a cooperative task, the two fields are configured with the same goal so that both chains act collaboratively. However, further modification is required to enforce a relative constraint between the manipulators to avoid crushing, twisting, or otherwise violating the volumetric properties of a held object. To enforce the desired cooperative kinematic constraint between the manipulators, we define and generate a secondary potential field $\Phi(z)$ whose task-space target is the shared object frame $\{O\}$. The gradient of this field, evaluated at the *i*th end-effector, provides a new spring force which acts in contrast to any relative offset between the manipulators. The new, modified gradient at the *i*th manipulator for APF control is calculated as:

$$\nabla_i = \frac{\partial \Psi_i(z_{ai})}{\partial z} + \frac{\partial \Phi(z_{ri})}{\partial z} \tag{1}$$

This arrangement can be understood in Figure 2. An important consideration: this research is using the Secant Method to create a trajectory in Cartesian space. As such, dynamic effects such as gravity and Coriolis effects do not need to be considered within the planner. These terms are accounted for in the arm controllers and in the force profile read by the sensors.

2.2 Incorporating Grasp Offset

To maintain coherent robot motion in cooperative mode, the gradients $\{\frac{\partial \Psi_1}{\partial z}, \frac{\partial \Psi_2}{\partial z}\}$ should be nominally evaluated at an identical location. This configuration would allow each manipulator to share a final link when invoking the inverse Jacobian, resulting in a common center of rotation for the combined manipulator. This is accomplished by establishing a *virtual Tool Center Point* (vTCP) for each manipulator, derived from the grasp transformation.

$$({}^{E}\boldsymbol{T}_V)_i = ({}^{O}\boldsymbol{T}_{Gi})^{-1} \tag{2}$$

In this manner, the robot end-effector will nominally coincide with the grasp feature while the vTCP will coincide with the object's body origin. While the vTCP is reserved as the last link in each kinematic chain, it is excluded from all obstacle avoidance calculations.

Finally, disturbances or errors may result in transitory or fixed offsets between the vTCPs, leaving the shared object frame ambiguously defined. We resolve the ambiguity by approximately inferring $\{O\}$ in real-time as the average of the vTCP poses. For the position component, this is easily computed as the element-wise mean of both. For the orientation component, we use the 50% quaternion spherical linear interpretation (SLERP) between the two orientations.

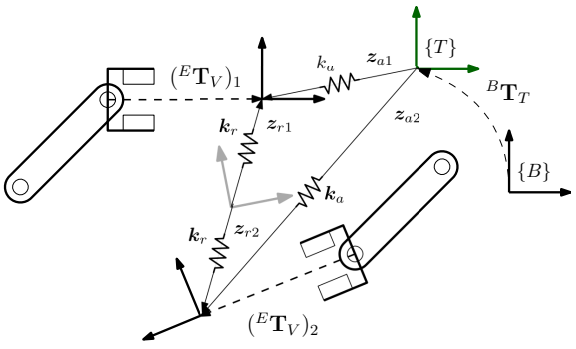

Figure 2: Dual-arm coordinated control.

3 COMPLIANCE CONTROL

3.1 Overview

Let a convention for generalized forces, or wrenches, be defined:

$$\boldsymbol{F}_x = \begin{bmatrix} \boldsymbol{f}_x^T & \boldsymbol{\tau}_x^T \end{bmatrix}^T \tag{3}$$

where the wrench is composed of a linear force $\boldsymbol{f}$ and a torque $\boldsymbol{\tau}$ applied at some point x.

Compliance can be implemented in an artificial potential field by superimposing a new class of forces onto the gradient of the map. The forces are constructed according to the laws

$$\boldsymbol{F}_{Ec} = \boldsymbol{k}_E \odot (\boldsymbol{F}_{Ed} - \boldsymbol{F}_E) \tag{4}$$

where $\boldsymbol{k}_E$ is a vector of gain factors whose entries correspond to each respective element of a generalized force vector, and which are applied to a wrench via the Hadamard product with the $\odot$ operator. $\boldsymbol{F}_E$ is the current *external* wrench applied to the object and $\boldsymbol{F}_{Ed}$ is the desired or commanded external wrench.

In the dual-arm condition, as in any similar cooperative manipulation task, an additional *internal* force is introduced as an artifact of its over-constrained nature. The internal force can be decomposed in a similar manner as to the external and with the same subscripted meanings:

$$\boldsymbol{F}_{Ic} = \boldsymbol{k}_I \odot (\boldsymbol{F}_{Id} - \boldsymbol{F}_I) \tag{5}$$

The integration of these two compliance forces into the APF controller is detailed in Figure 3. The subsequent sections investigate how to accurately determine $\boldsymbol{F}_E$ and $\boldsymbol{F}_I$.

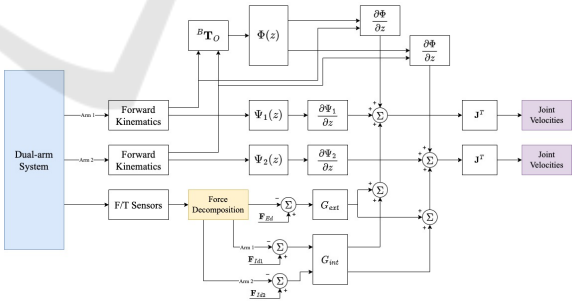

Figure 3: Dual-arm coordinated and compliant control.

3.2 F/T Equivalence

In these operations, it is often necessary to convert forces from one point of application to another while maintaining an equivalent effect on the rigid body. This requirement is most often introduced when a manipulator's force-torque sensor does not coincide with the tool center point, as will be the case in cooperative manipulation tasks involving a volumetric object.

The matrix transferring a spatial wrench at point α to point β is

$$^{\gamma}\mathbf{\Omega}_{\alpha} = \begin{bmatrix} \boldsymbol{I}_3 & \mathbf{0}_3 \\ \lfloor \boldsymbol{r}_{\gamma\to\alpha}\times \rfloor & \boldsymbol{I}_3 \end{bmatrix} \tag{6}$$

where $\lfloor\cdot\times\rfloor$ forms the skew-symmetric matrix for cross-product operations and $\boldsymbol{r}_{\gamma\to\alpha}$ is the vector drawn from the point γ to the point α.

Where it is necessary to perform a change of basis from $\{A\}$ to $\{B\}$, it shall be noted as $\boldsymbol{x}_B = {}^B\boldsymbol{\beta}_A\boldsymbol{x}_A$. Unless otherwise stated, we express all vectors and wrenches in a fixed common work frame $\{W\}$.

3.3 Determining External Force

The analysis completed by (Walker et al., 1991) of a rigid body assumes a firm grasp transmits both forces and moments at the point of contact. Let $\boldsymbol{F}_{gi}$ be the contact forces at the ith of k total grasp points expressed in work frame coordinates. From a free-body diagram analysis, the net force exerted externally on the object can be expressed generally as

$$\boldsymbol{F}_o = \boldsymbol{W}\boldsymbol{F}_g \tag{7}$$

with

$$\boldsymbol{F}_g = [\boldsymbol{F}_{g1}^T, ..., \boldsymbol{F}_{gk}^T]^T \tag{8}$$

$$\boldsymbol{W} = \begin{bmatrix} \boldsymbol{I}_3 & \mathbf{0}_3 & \dots & \boldsymbol{I}_3 & \mathbf{0}_3 \\ \lfloor r_{g1}\times\rfloor & \boldsymbol{I}_3 & \dots & \lfloor r_{gk}\times\rfloor & \boldsymbol{I}_3 \end{bmatrix} \tag{9}$$

where $\boldsymbol{W}$ is known as the grasp matrix in the R^3 spatial context, r_{gi} is the vector drawn from the object frame to the ith grasp point, and all vectors are expressed in the common work frame.

We further stipulate that the force-torque sensor might not be coincident with the end-effector of the robot chain. Therefore, so as to calculate forces as applied at the sensor, we replace the vectors r_{gi} with r_{si}, the vector drawn from the object frame to the ith chain's F/T sensor. In this way, the end-effector chain is considered a rigid component of the grasped object, and the net object force can be expressed as a function of the F/T sensor readings $\boldsymbol{F}_{ri}$. In the dual-arm scenario shown in Figure 4, these relationships reduce to

$$\boldsymbol{F}_o = \bar{\boldsymbol{W}}\boldsymbol{F}_r \tag{10}$$

with

$$\boldsymbol{F}_r = \begin{bmatrix} \boldsymbol{F}_{r1}^T & \boldsymbol{F}_{r2}^T \end{bmatrix}^T \tag{11}$$

$$\bar{\boldsymbol{W}} = \begin{bmatrix} {}^O\mathbf{\Omega}_{S1} & {}^O\mathbf{\Omega}_{S2} \end{bmatrix} \tag{12}$$

In general, the external force $\boldsymbol{F}_o$ includes not only external loads but also the effects of gravity and any dynamic forces arising from the acceleration of the body. This is observed from the sum of forces and moments for a dynamic rigid body with constant mass

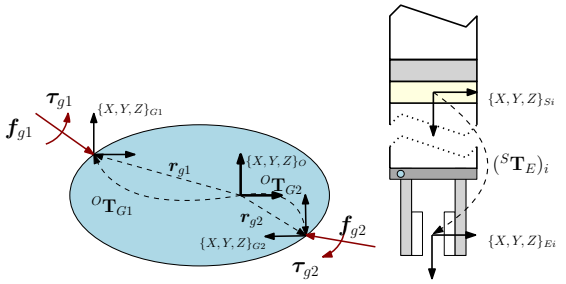

(a) (b)

Figure 4: (a) Dual-arm cooperative object detail. (b) End-effector chain detail.

and inertial properties. However, a rigorous consideration of inertial effects is not the focus of the present investigation. We assume small acceleration and velocity throughout, resulting in small dynamical terms in comparison to external disturbances. As the incorporation of the dynamical terms is linear, they can thus be neglected. We also consider the effect of gravity as an external disturbance rather than accounting for it directly, since the mass of the object is unknown. In practice, zeroing of $\boldsymbol{F}_o$ suffices to account for gravity, and we establish:

$$\boldsymbol{F}_E = \boldsymbol{F}_o \tag{13}$$

3.4 Determining Internal Force

Established methods in literature isolate the internal force contribution of a given manipulator by subtracting the expected wrench $\bar{\boldsymbol{F}}_{ri}$ in an unloaded internal condition from the reported wrench.

$$\boldsymbol{F}_{int} = \boldsymbol{F}_r - \bar{\boldsymbol{F}}_r \tag{14}$$

To obtain $\bar{\boldsymbol{F}}_r$, the authors have pre-multiplied (10) by the inverse of the grasp matrix to isolate $\boldsymbol{F}_r$. However, in over-constrained systems, the grasp matrix has a nonzero null space and cannot be inverted except approximately by a pseudoinverse, as investigated in (Walker et al., 1991). These linear approximations are merely mathematical optimizations rather than informed studies, resulting in poor accuracy along certain axes.

Rather than make use of a pseudoinverse, we propose modeling the handled object as a statically indeterminate beam. This model assumes the object has a fairly uniform cross-section and structural stiffness. In the case of transverse forces and moments (Figure 5), the one-dimensional reactionary wrench at the constraint a units away from the external wrench application upon a beam of length l can be calculated according to (Roark et al., 2012).

$$R_{T,a}(f,\tau) = \frac{-f}{l^3}(l-a)^2(l+2a) + \frac{6\tau a}{l^3}(l-a) \tag{15}$$

$$M_{T,a}(t,\tau) = \frac{fa}{l^2}(l-a)^2 + \frac{\tau}{l^2}(l^2 - 4al + 3a^2) \quad (16)$$

where R is the linear reactionary force, M is the reactionary torque, f is the load force, and τ is the load torque.

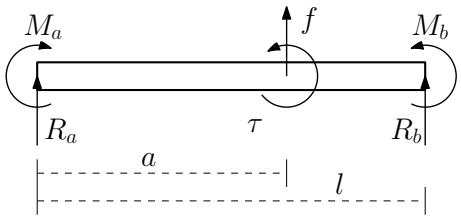

Figure 5: Statically indeterminate beam (transverse forces).

The longitudinal case (Figure 6) may be similarly calculated (Hibbeler, 2011).

$$R_{L,a}(f) = f\left(\frac{a-l}{l}\right) \quad (17)$$

$$M_{L,a}(\tau) = \tau\left(\frac{a-l}{l}\right) \quad (18)$$

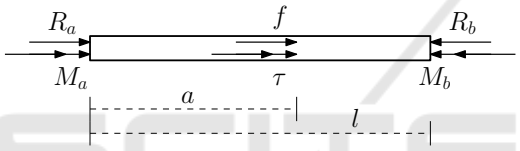

Figure 6: Statically indeterminate beam (longitudinal forces).

The question now arises as to which physical points should be associated with the ends of the modeled beam, or *beam phantom*. An intuitive option is to define the beam phantom as the line joining the two grasp points. However, the end-effector chains themselves can be seen as forming part of a larger rigid body containing the shared object. Here, the nuances of the manipulation problem can become more relevant, such as the comparative stiffness of the object and end-effector chain. We proceed with a method based on the second observation and assume a more accurate model admits to the entire structure contributing to the combined deformation effects. The force-torque sensors of either arm shall be the termination points of the beam phantom, with the span of the vector $\boldsymbol{g}$ joining them termed the *grasp line* (Figure 7).

The phantom point of force application $\{\tilde{O}\}$ is defined by orthogonal projection of the object origin onto the grasp line. In this way, the equivalent offset a is maintained, which is critical for model validity.

$$\boldsymbol{r}_{\tilde{o}} = \text{Proj}_{\boldsymbol{g}}(\boldsymbol{r}_o) = \frac{\boldsymbol{g}^T\boldsymbol{r}_o}{\boldsymbol{r}_o^T\boldsymbol{r}_o}\boldsymbol{r}_o \quad (19)$$

$$\{a,l\} = \{||\boldsymbol{r}_{\tilde{o}}||, ||\boldsymbol{g}||\} \quad (20)$$

where $\boldsymbol{r}_o$ is the vector drawn from the F/T sensor of manipulator 1 to the shared object center O. Additionally, $\{\tilde{O}\}$ is oriented so as to always align its x-axis with the longitudinal axis of the beam. Since internal forces do not affect object motion and thus do not appear in the net object force $\boldsymbol{F}_o$, the result of (10) may be used for the purpose of calculating the expected wrenches in the internally unloaded condition. The object force is transferred to $\{\tilde{O}\}$ by F/T equivalence, and then expressed in the coordinates of $\{\tilde{O}\}$, allowing systematic application of the beam equations with resultant wrenches $\tilde{\boldsymbol{F}}_r$ expressed in the same frame.

$$\boldsymbol{F}_{\tilde{o}} = {}^{\tilde{O}}\boldsymbol{\beta}_W\,{}^{\tilde{O}}\boldsymbol{\Omega}_O\boldsymbol{F}_o \quad (21)$$

$$\tilde{\boldsymbol{F}}_{r1} = \begin{bmatrix} R_{L,a}(\boldsymbol{f}_{\tilde{o}}\cdot\hat{\imath}) \\ R_{T,a}(\boldsymbol{f}_{\tilde{o}}\cdot\hat{\jmath}, \boldsymbol{\tau}_{\tilde{o}}\cdot\hat{k}) \\ -R_{T,a}(-\boldsymbol{f}_{\tilde{o}}\cdot\hat{k}, \boldsymbol{\tau}_{\tilde{o}}\cdot\hat{\jmath}) \\ M_{L,a}(\boldsymbol{\tau}_{\tilde{o}}\cdot\hat{\imath}) \\ -M_{T,a}(-\boldsymbol{f}_{\tilde{o}}\cdot\hat{k}, \boldsymbol{\tau}_{\tilde{o}}\cdot\hat{\jmath}) \\ -M_{T,a}(\boldsymbol{f}_{\tilde{o}}\cdot\hat{\jmath}, \boldsymbol{\tau}_{\tilde{o}}\cdot\hat{k}) \end{bmatrix} \quad (22)$$

where $\hat{\imath}, \hat{\jmath}, \hat{k}$ are the unit identity vectors. Note that, in practice, care must be taken to properly account for sign differences caused by the coordinate convention.

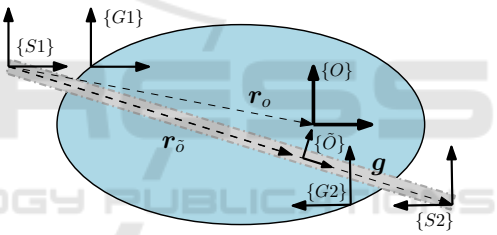

Figure 7: Statically indeterminate beam phantom.

It is desirable to compute compliance in the object-fixed frame. This permits, for instance, a constant squeeze force along a particular axis of the object, regardless of its orientation or that of the end-effectors with respect to it. Therefore, before the gain factors are applied, $\tilde{\boldsymbol{F}}_{ri}$ is transferred to and expressed in the original object frame, $\{O\}$.

$$\bar{\boldsymbol{F}}_{r1} = {}^{O}\boldsymbol{\beta}_W\,{}^{O}\boldsymbol{\Omega}_{\tilde{O}}\,{}^{W}\boldsymbol{S}_{\tilde{O}}\tilde{\boldsymbol{F}}_{r1} \quad (23)$$

Note that it has not been necessary to perform identical calculations on the second manipulator. This is because, by definition, internal forces do not contribute to object motion. If the internal forces contributed by the ith manipulator are transferred to and expressed in the same frame, then

$$\Sigma\bar{\boldsymbol{F}}_{Ii} = \boldsymbol{0} \quad (24)$$

Since there are only two manipulators, this expands to

$$\bar{\boldsymbol{F}}_{I1} = -\bar{\boldsymbol{F}}_{I2} \quad (25)$$

The internal gain factors $\boldsymbol{k}_I$ are applied and the results expressed in work frame coordinates.

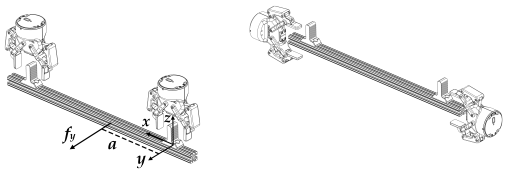

(a) (b)

Figure 8: (a) Experiment upright posture. (b) Experiment horizontal posture.

4 FORCE DECOMPOSITION EXPERIMENTS

To illustrate the advantage of our beam method, static experiments are performed on a mock object manipulation problem. The object is a 1" aluminium extrusion and is grasped by 2-finger grippers with approximately 470 mm of separation. F/T readings are recorded by an ATI Axia80 placed in the end-effector chain of one of the manipulators. It should be mentioned that the finger grippers will always provide forces, but due to their relatively small contact surface, may not provide reactionary torques along all axes. To help determine the true boundary conditions, two different grasp postures are evaluated (Figure 8). The *upright* posture minimizes the gripper surface area that would contribute a torque in the z-axis, while the *horizontal* posture maximizes it. Linear force along the y-axis and torque along the z-axis are independently applied at seven different points along the beam. The measured F/T response is compared to the expected values yielded by the Moore-Penrose pseudoinverse (PINV), the No-Squeeze pseudoinverse (Walker et al., 1991), our beam method, and a simply-supported (SS) model. The simply-supported model assumes the grippers transmit no torque; by removing the torque entries of $\boldsymbol{F}_r$, the grasp matrix $\boldsymbol{W}$ becomes square with a unique non-approximate inverse. As anticipated, the simply-supported model best predicts experimental F/T readings in the upright configuration; however, our beam method provides substantial improvements in the horizontal posture, as shown in Table 1.

First, it is noted that the beam and pseudoinverse predictions for $\boldsymbol{f}_r$ in response to a linear force converge when the point of force application is near the geometric center of beam. In this regard, the beam method provides the greatest advantage when the shared object has a center of gravity which does not coincide with its volumetric center, or when it has an off-center interface point with the environment.

The experiments yield one modification that must be made: both manipulators share equally the load induced by a linear force applied longitudinally along the beam (that is, along the denoted x-axis), regardless of where it is applied. While the beam method theory is in disagreement, it is simple to revise it to accommodate:

$$R'_{L,a}(f) = f\left(\frac{-1}{2}\right) \tag{26}$$

Table 1: Minimum and maximum F/T sensor prediction error ϵ, as a percentage of $|\boldsymbol{F}_{ext}|$, in response to a static load applied at a range of locations $\pm 20\%$ of the distance between the sensors in the horizontal posture. Lower is better.

Isolated Force				
ϵ	PINV	No-Squeeze	SS	Beam
f_r	1.5—31	2.6—36	1.9—17	0.9—8.7
τ_r	2.4—30	3.3—33	5.7—22	0.0—5.1

Isolated Torque				
ϵ	PINV	No-Squeeze	SS	Beam
f_r	88—140	110—160	19—74	6.5—47
τ_r	64—81	76—92	26—42	5.2—31

5 LIVE APPLICATION ANALYSIS

A typical benchmark for manipulation tasks is the peg-in-hole problem, serving as a primary primitive for applied multi-axis compliance in insertion contexts. To benchmark our dual-arm system with improved force decomposition, we design a peg-in-hole problem (Figure 9) in which both internal and external compliance are required along a transverse axis. Internal compliance may be necessary when the expected and actual object geometries do not match, which we simulate by using object handles misaligned by about 40 mm. To highlight the advantage of the beam method, the mating point is located non-centrally between the two manipulators, at a point 20% along the total length. To demonstrate external compliance, the mating peg location is erroneously perturbed, and a large 45° chamfer is added to the peg sockets to lengthen the distance over which compliance is employed. Additionally, the use of two separate mating features provide a rotational constraint to demonstrate both linear and angular responses. The mating point is taken as the center-point between the two features.

Our dual-arm system is comprised of two UR5e collaborative robot arms, each attached to a respective rail carriage to form a total of 14 DoF. The rail carriages are individually powered by Parker-Hannifin

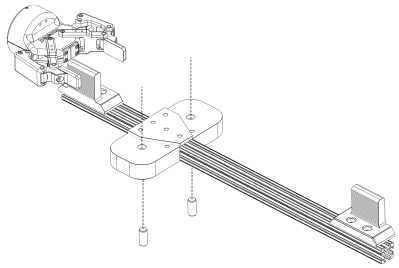

Figure 9: Aluminium extrusion with misaligned handles and two peg sockets. Beam length is not to scale in this sketch.

IPA04-HC motor controllers. F/T readings for each manipulator are obtained using the internal UR5e sensors. Manipulator 1 uses a Robotiq 2F-85 gripper, and manipulator 2 uses a longer 2F-140 model. To ensure the transmission of torque at the grasp points, the object is grasped in a horizontal posture.

5.1 Isolated Force Application

We simulate the interactions between the peg and hole by applying a transverse force f_y at the mating point. The metrics of interest are the reported internal force $f_{int,y}$ and torque τ_z. Since only an external force is in fact being applied during the experiment, $f_{int,y}$ and $\tau_{int,z}$ should remain constant. For completeness, this experiment is performed twice, once with external control enabled and again with it disabled. When enabled, the same control gains are used across the tested force decomposition methods. It is noted that the baseline internal force caused by gripping the misaligned handles varies depending on the force decomposition method employed. This is accounted for by subtracting the prior baseline reading before analysis.

Table 2: Maximum internal force and torque in response to a simulated peg-in-hole interaction with the Beam method and control disabled. Lower is better.

Component (as % of $\lvert \boldsymbol{F}_{ext} \rvert$)	Method PINV	No-Squeeze	Beam
Linear, f_{int}	15	16	0.8
Torque, τ_{int}	13	15	4.1

From Tables 2 and 3, it is clear that the beam method provides an improvement in registered internal loading in all conditions, with maximum benefit when the control gains are lowest (emulated at the limit by disabled control). Improvements over the Moore-Penrose pseudoinverse are maximum at 18x in linear force and 3x in torque. Against the No-Squeeze method, the Beam technique offers maximum improvements of 15x in force and 3x in torque.

Table 3: Maximum internal force and torque in response to a simulated peg-in-hole interaction with the Beam method and control enabled. Lower is better.

Component (as % of $\lvert \boldsymbol{F}_{ext} \rvert$)	Method PINV	No-Squeeze	Beam
Linear, f_{int}	3.5	4.5	1.1
Torque, τ_{int}	10	20	5.9

5.2 Peg-in-Hole Demonstration

The complete system is run on actual hardware with control enabled. The purpose of the demonstration is to show the collective functioning of the planner and compliance technique in the real-world context of a mating problem. Figure 9 is a still frame from the demonstration recording. The demonstration successfully mates the rotationally constrained object with an initial error neighboring 6° in rotation and 2.5 cm in vertical distance. The direct-contact insertion phase completes in approximately five seconds. Greater error could be tested using larger socket chamfers. Oscillations are present once both pegs fully thread into the sockets, particularly along the axis of the rail carriages. This is a stability problem associated with the force impulses upon contact with a rigid surface. Reducing the force response gain and increasing positional stiffness alleviates these oscillations.

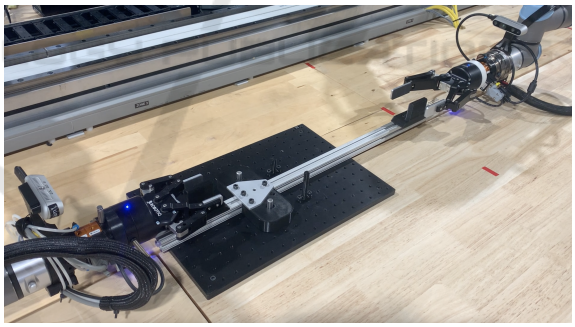

Figure 10: Dual peg-in-hole demonstration.

6 CONCLUSION

Coordinated dual-arm control of a shared object has been achieved using a modified artificial potential field controller as the basis for path planning. For demonstration, the system was able to solve an angularly constrained, non-central peg-in-hole problem. Future work may involve demonstrating static and dynamic object collision avoidance, leveraging the novel capabilities of the Secant Method. Moreover, compliance has been incorporated into the controller using a physically driven nonlinear model. Our

method of force decomposition achieves better results in experiment, up to an order of magnitude, than common methods in literature. Future improvements to the technique could include modeling interaction torques as a force-couple with known moment arm rather than a concentrated torque; this would match the physical scenario more closely in certain configurations. Internal compliance might also be adjusted so as to use each manipulator's gripper point as the respective center of rotation, while still sharing the object center for external compliance and object-level trajectory planning. Object mass and inertia properties, neglected here, could be incorporated into the equations of motion. A Kalman filter could be explored for smoothing reactions to impulsive contact forces and reducing oscillations. Taken together, this work forms the basis for future dual-arm collaborative object manipulation, including the exploration of intelligent insertion strategies to improve speed and repeatability.

REFERENCES

Ahlin, K. J., Sadegh, N., and Hu, A.-P. (2018). The secant method: Global trajectory planning with variable radius, solid obstacles. In *Dynamic Systems and Control Conference*, volume 51913, page V003T32A015. American Society of Mechanical Engineers.

Calanca, A., Muradore, R., and Fiorini, P. (2016). A review of algorithms for compliant control of stiff and fixed-compliance robots. *IEEE/ASME Transactions on Mechatronics*, 21(2):613–624.

Erhart, S. and Hirche, S. (2015). Internal force analysis and load distribution for cooperative multi-robot manipulation. *IEEE Transactions on Robotics*, 31(5):1238–1243.

Gao, M., Zhou, H., Yang, Y., Dong, Z., and He, Z. (2022). An intelligent master–slave collaborative robot system for cafeteria service. *Robotics and Autonomous Systems*, 154:104121.

Hibbeler, R. C. (2011). *Mechanics of materials*. Prentice Hall, Boston, 8th ed edition.

Hu, B., Yan, L., Han, L., and Yu, H. (2021). Coordinated compliance control of dual-arm robot astronaut for payload operation. *International Journal of Advanced Robotic Systems*, 18(3):17298814211012850.

Khatib, O. (1985). Real-time obstacle avoidance for manipulators and mobile robots. In *Proceedings. 1985 IEEE international conference on robotics and automation*, volume 2, pages 500–505. IEEE.

Khatib, O. (1986). The potential field approach and operational space formulation in robot control. pages 367–377. Springer.

Kim, R., Balakirsky, S., Ahlin, K., Marcum, M., and Mazumdar, A. (2021). Enhancing payload capacity with dual-arm manipulation and adaptable mechanical intelligence. *Journal of Mechanisms and Robotics*, 13(2).

Kousi, N., Michalos, G., Aivaliotis, S., and Makris, S. (2018). An outlook on future assembly systems introducing robotic mobile dual arm workers. *Procedia CIRP*, 72:33–38. 51st CIRP Conference on Manufacturing Systems.

LaValle, S. M. (2006). *Planning algorithms*. Cambridge university press.

Omar, R., Sabudin, E., CK, C. K. M., et al. (2016). Potential field methods and their inherent approaches for path planning. volume 11, pages 10801–10805. Asian Research Publishing Network (ARPN).

Ren, X., Huang, L., and Zhao, M. (2021). Prioritized hierarchical compliance control for dual-arm robot stable clamping.

Roark, R. J., Young, W. C., Budynas, R. G., and Sadegh, A. M. (2012). *Roark's formulas for stress and strain*. McGraw-Hill, New York, 8th ed edition. OCLC: ocn769455976.

Seraji, H. (1994). Adaptive admittance control: an approach to explicit force control in compliant motion. In *Proceedings of the 1994 IEEE International Conference on Robotics and Automation*, pages 2705–2712 vol.4.

Song, X., Huang, H., Xu, W., and Li, B. (2022). A robust force controller of multi-robot cooperative manipulators for carrying task. In *2022 IEEE International Conference on Robotics and Biomimetics (ROBIO)*, pages 987–992, Jinghong, China. IEEE.

Song, X., Mao, H., Huang, H., Xu, W., and Li, B. (2021). A Dynamic Adaptive Impedance Controller for Force Tracking of Dual-arm Manipulators in Uncertain Contact Environment. In *2021 IEEE International Conference on Robotics and Biomimetics (ROBIO)*, pages 1674–1681, Sanya, China. IEEE.

Walker, I. D., Freeman, R. A., and Marcus, S. I. (1991). Analysis of Motion and Internal Loading of Objects Grasped by Multiple Cooperating Manipulators. *The International Journal of Robotics Research*, 10(4):396–409.

Wolf, S., Grioli, G., Eiberger, O., Friedl, W., Grebenstein, M., Hoppner, H., Burdet, E., Caldwell, D. G., Carloni, R., Catalano, M. G., Lefeber, D., Stramigioli, S., Tsagarakis, N., Van Damme, M., Van Ham, R., Vanderborght, B., Visser, L. C., Bicchi, A., and Albu-Schaffer, A. (2016). Variable stiffness actuators: Review on design and components. *IEEE/ASME Transactions on Mechatronics*, 21(5):2418–2430. Cited By :266.

Xian, Z., Lertkultanon, P., and Pham, Q.-C. (2017). Closed-chain manipulation of large objects by multi-arm robotic systems. *IEEE Robotics and Automation Letters*, 2(4):1832–1839.